Ahmed A, Tiwari R, Strangeways HJ, Dlay S, Johnsen MG. Wavelet-based Analogous Phase Scintillation Index for High Latitudes. *Space Weather* 2015, 10.1002/2015SW001183

AGU PUBLICATIONS

Space Weather

RESEARCH ARTICLE
10.1002/2015SW001183

Key Points:
- Wavelet-based improved analogous phase scintillation index
- Scintillation determination based on rate of change of TEC
- Determining phase scintillation using raw TEC data at 1 Hz

Correspondence to:
A. Ahmed,
arslan.ahmed90@gmail.com

Citation:
Ahmed, A., R. Tiwari, H. J. Strangeways, S. Dlay, and M. G. Johnsen (2015), Wavelet-based analogous phase scintillation index for high latitudes, *Space Weather*, *13*, doi:10.1002/2015SW001183.

Received 12 MAR 2015
Accepted 7 JUL 2015
Accepted article online 14 JUL 2015

Wavelet-based analogous phase scintillation index for high latitudes

A. Ahmed[1], R. Tiwari[1], H. J. Strangeways[1], S. Dlay[1], and M. G. Johnsen[2]

[1]School of Electrical and Electronic Engineering, University of Newcastle upon Tyne, Newcastle upon Tyne, UK, [2]Tromsø Geophysical Observatory, University of Tromsø, Tromsø, Norway

Abstract The Global Positioning System (GPS) performance at high latitudes can be severely affected by the ionospheric scintillation due to the presence of small-scale time-varying electron density irregularities. In this paper, an improved analogous phase scintillation index derived using the wavelet-transform-based filtering technique is presented to represent the effects of scintillation regionally at European high latitudes. The improved analogous phase index is then compared with the original analogous phase index and the phase scintillation index for performance comparison using 1 year of data from Trondheim, Norway (63.41°N, 10.4°E). This index provides samples at a 1 min rate using raw total electron content (TEC) data at 1 Hz for the prediction of phase scintillation compared to the scintillation monitoring receivers (such as NovAtel Global Navigation Satellite Systems Ionospheric Scintillation and TEC Monitor receivers) which operate at 50 Hz rate and are thus rather computationally intensive. The estimation of phase scintillation effects using high sample rate data makes the improved analogous phase index a suitable candidate which can be used in regional geodetic dual-frequency-based GPS receivers to efficiently update the tracking loop parameters based on tracking jitter variance.

1. Introduction

The electron density irregularities in the ionosphere causes amplitude and phase fluctuations in the signals transiting the ionosphere which result in signal degradation and may lead to loss of lock in the GPS (Global Positioning System) receiver if the amplitude and/or phase fluctuations, also termed ionospheric scintillation, are deep, frequent, and of sufficient time duration. The scintillation effects are rather more severe, particularly at high latitudes [*Aarons*, 1997; *Doherty et al.*, 2000; *Skone et al.*, 2008, 2009; *Tiwari et al.*, 2010, 2011a] and also near equatorial latitudes [*Aarons*, 1977; *Xu et al.*, 2012] during a geomagnetic storm. Ionospheric scintillation can be classified as amplitude scintillation quantified by the S_4 index (unitless) and phase scintillation index σ_ϕ (measured in radians). Amplitude scintillations are more likely to occur at low-latitude regions ($\pm 15°$ geomagnetic latitude) and are caused when a signal passing through the irregular electron density in the ionosphere experiences small-angle scattering [*Aarons*, 1997; *Kintner et al.*, 2007]. Phase scintillation, on the other hand, is more dominant at high latitudes and the polar caps [*Kersley et al.*, 1988; *Tiwari et al.*, 2010], can last for long periods of time, and may lead to loss of phase lock within the receiver [*Datta-Barua et al.*, 2003; *Seo et al.*, 2009; *Knight*, 2000]. Phase scintillations are produced near the first Fresnel radius ($r_F/\sqrt{2}$) at small wave numbers [*Kintner et al.*, 2007] where $r_F = \sqrt{2\lambda z}$ is the Fresnel radius (z is the distance between the ionosphere irregularities and receiver; λ is the wavelength). The spectrum of the received phase deviations based on the phase screen approximation [*Beach and Kintner*, 1999] $\Phi_P(q)$ can be given as

$$\Phi_P(q) = \Phi_\phi(q) \cos\left(\frac{q^2 r_F^2}{8\pi}\right) \tag{1}$$

where q is the horizontal wave number of the phase fluctuations across the phase screen, $\Phi_\phi(q)$ is the power spectrum of the phase exciting the phase screen, and ϕ represents the phase deviations. In equation (1), the phase deviations on a phase screen may approximately be estimated by the fast time variations of the total electron content (TEC) present along the signal path through the time derivative of TEC

[*Beach and Kintner*, 1999; *Jakowski et al.*, 2012; *Basu et al.*, 1999]. The TEC is usually estimated by the integral of the electron density present along the signal path using the range delay equation [*Garner et al.*, 2008]:

$$I = \frac{q^2}{2c\epsilon m_e f(2\pi)^2} \int_{\text{path}} N_e \mathrm{d}l \tag{2}$$

$$I = \frac{q^2}{2c\epsilon m_e f(2\pi)^2} \mathrm{TEC} \tag{3}$$

where $\mathrm{TEC} = \int_{\text{path}} N_e \mathrm{d}l$, q is the charge of an electron, m_e is the mass of an electron, c is the speed of light, f is the carrier frequency of the signal in hertz, and ϵ is the permittivity of free space. From *Garner et al.* [2008], the TEC at the receiver can be estimated by using the dual-frequency GPS observations given by equations (4) and (5)

$$\mathrm{TEC} = \frac{f_1^2 f_2^2}{40.3\left(f_2^2 - f_1^2\right)}(P_1 - P_2) \tag{4}$$

$$\mathrm{TEC} = \frac{-f_1^2 f_2^2}{40.3\left(f_2^2 - f_1^2\right)}(\Phi_1 - \Phi_2) \tag{5}$$

where P_1 and P_2 are the pseudoranges and Φ_1 and Φ_2 are the phase observations of the GPS $L1$(1575.42 MHz) and $L2$(1227.6 MHz) frequencies. It should be noted that the TEC measurements made using the above equations are for the slant path and can be converted to vertical TEC (VTEC) using equation (6):

$$\mathrm{VTEC} = \frac{1}{M(E)} \times \mathrm{TEC} \tag{6}$$

where $M(E)$ is the mapping function given in equation (7), used for estimating the VTEC by assuming an approximate ionospheric pierce point height (h_{IPP}) of 350 km. The mapping function depends on the elevation angle E.

$$M(E) = \left(1 - \left(\frac{R_E \cos^2 E}{R_E + h_{\mathrm{IPP}}}\right)\right)^{-1/2} \tag{7}$$

where R_E is the radius of the Earth (6378.1 km) and h_{IPP} is the ionospheric pierce point (IPP) height considered as 350 km. Several researchers [*Basu et al.*, 1999; *Krankowski et al.*, 2005; *Guozhu et al.*, 2008] have shown a strong correlation between the scintillation indices and the rate of change of TEC (ROT), and therefore ROT has been used extensively to relate the phase fluctuations with the TEC variations due to ionospheric irregularities. A very good overview of the scintillation activity based on TEC variations is given by *Prikryl et al.* [2013] where the author has generated maps of the TEC activity using Canadian High Arctic Ionospheric Network GPS receivers at various latitudes and a comparison is also made by estimating the phase scintillation intensity using the phase scintillation index derived using the 50 Hz data and a proxy index derived using the 1 Hz data. *Ghoddousi-Fard et al.* [2013] suggested that based on their availability, the regionally based geodetic receivers operating at 1 Hz could be far better to study the ionospheric scintillation activity. In this regard, *Tiwari et al.* [2013] used the TEC-based observations from dual-frequency GPS receivers to design a new TEC-based phase scintillation index $\sigma_{\phi a}$ which appeared to be a good candidate to represent the phase scintillation activity for European high latitudes and can serve as a substitute for the phase scintillation index σ_ϕ due to the shown strong correlation between $\sigma_{\phi a}$ and σ_ϕ. The main advantage of using $\sigma_{\phi a}$ is that it uses time and spatial variations of TEC at 1 Hz using the dual-frequency ($L1$ and $L2$) GPS observations to represent the phase deviations compared to the ordinary scintillation receivers which employ low sample rate data (50 Hz) for quantifying the phase scintillation values. The $\sigma_{\phi a}$ can be conveniently used in software GPS receivers for estimating the tracking error variance to update the tracking loop parameters.

In this paper, an improved analogous phase scintillation index $\sigma_{\phi a}^{\mathrm{w}}$ is proposed by using a wavelet-transform-based filtering. The performance of the proposed index is verified by using data from one of the receiver stations from European high latitudes to use this index to represent the regional phase scintillation activity. In future, this index can be used regionally at European high latitudes to mitigate the phase scintillation effects on GPS receivers if used to estimate the tracking error variance. This paper is divided into two main

sections. In the first section, the wavelet-transform-based filtering is used to propose the improved analogous phase index $\sigma^{w}_{\phi a}$, and in the second part, its performance is validated by using the GPS data under different geomagnetic conditions and is then compared with the original analogous phase index $\sigma_{\phi a}$ and the phase scintillation index σ_{ϕ} .

2. Improved Analogous Phase Index

In *Tiwari et al.* [2013], the analogous phase index is given as

$$\sigma_{\phi a} = \left[\varpi \left(\chi (M), v_p \right) \times \sigma_{\mathrm{VTEC}'_{\mathrm{HPF}}} \right] \tag{8}$$

where $\varpi(\chi(M), v_p)$ is the weight function in equation (9) used to achieve independence from the elevation angle by assuming a single-layer ionosphere. The $\varpi(\chi(M), v_p)$ is a function of $\chi(M)$ and the IPP velocity V_p. The $\chi(M)$ is the mapping function between two consecutive epochs i and $i+1$ given in equation (10).

$$\varpi \left(\chi (M), v_p \right) = \frac{2\pi S 40.3}{cf} \times \left[\chi (M), v_p \right] \tag{9}$$

where

$$\chi (M) = \frac{1}{\left(M_i(E) M_{i+1}(E) \right)^2} \tag{10}$$

In equation (9), S is the distance of the slant path from the receiver to the phase screen. Referring to equation (8), $\sigma_{\mathrm{VTEC}'_{\mathrm{HPF}}}$ is the standard deviation of the high-pass-filtered $\mathrm{VTEC}'_{\mathrm{HPF}}$ where $\mathrm{VTEC}'_{\mathrm{HPF}}$ is given below

$$\mathrm{VTEC}'_{\mathrm{HPF}} = \left[M \left\{ \frac{\partial \mathrm{TEC}}{\partial x} v_p + \frac{\partial \mathrm{TEC}}{\partial t} \mathrm{d}t \right\} + \mathrm{TEC} \frac{\Delta M}{\Delta t} \right]_{\mathrm{HPF}} \tag{11}$$

where $M = 1/M(E)$. In equation (11), the VTEC' depends on the partial derivative of TEC with respect to time t and distance x where x is the horizontal motion of IPP toward x. In equation (11), a second-order Butterworth high-pass filtering (HPF) with a cutoff frequency of 0.1 Hz was used to remove the slower fluctuations due to the slowly varying background ionosphere, satellite and receiver clock errors, Doppler shift, etc. It is mentioned by several researchers [*Forte*, 2005, 2007; *Mushini et al.*, 2012] that the phase scintillation indices at high latitudes are sensitive to filtering using time-invariant digital high-pass filters and hence result in overestimation or underestimation of the scintillation values. Usually, the actual cutoff frequency should be based on the Fresnel frequency F_f ($F_f = V_r/\sqrt{2\lambda z}$), but it is difficult to calculate the value of the irregular drift velocity V_r and z at every given location [*Mushini et al.*, 2012]. Therefore, most Global Navigation Satellite Systems Ionospheric Scintillation and TEC Monitor (GISTM) receivers use a cutoff frequency of 0.1 Hz which was first used for detrending the GPS data at middle and low latitudes [*Van Dierendonck et al.*, 1993; *Van Dierendonck and Arbesser-Rastburg*, 2004] and later used in scintillation receivers for quantifying the scintillation indices (amplitude and phase).

Forte [2005, 2007] and *Mushini et al.* [2012] have highlighted the problem of using high and low cutoff frequencies in dealing with raw GPS data and discussed this in detail. It was indicated by *Forte* [2005] that the drift velocity of the electron density irregularities at high latitudes can be much higher than at low latitudes and hence much higher Fresnel frequencies can be encountered at high latitudes. Therefore, using a default cutoff frequency of 0.1 Hz may not be appropriate to represent the true scintillation events for high-latitude data. On the other hand, several case studies were also presented in *Forte* [2005, 2007], where it is shown that using a high cutoff frequency would result in a wrong interpretation of the scintillation values. A new scintillation index S_{ϕ} was also proposed by *Forte* [2005] in which phase was detrended using high-pass filter with cutoff frequencies greater than 0.1 Hz and scintillation values were estimated using the standard deviation of phase rate of change over a 1 min interval. This S_{ϕ} index was then found to be a reliable index for representing phase variations at high latitudes.

In order to obviate the use of a HPF, several researchers [*Materassi and Mitchell*, 2007, 2009; *Tiwari et al.*, 2011b; *Mushini et al.*, 2012; *Niu et al.*, 2012] have successfully used the wavelet transform in signal detrending for determining the amplitude and phase scintillation indices using single frequency GPS $L1$ raw observations at 50 Hz. In this regard, a new scintillation index σ_{CHAIN} was also proposed by *Mushini et al.* [2012] using wavelet filtering.

The main problem in using the wavelet transform as a filtering technique for determining the scintillation indices (σ_ϕ, S_4, σ_{CHAIN}, and S_ϕ) is the use of low sample rate data (e.g., 50 Hz) which may not be optimum due to the high computational cost involved in the wavelet transform. Since $\sigma_{\phi a}$ uses high sample rate values (1 Hz), this is not such a problem in case of the analogous phase index $\sigma_{\phi a}$. Therefore, in deriving $\sigma_{\phi a}$ we used a wavelet-based filtering in equation (11) to remove the slower TEC fluctuations due to the varying background ionosphere, Doppler shift, satellite/receiver motion, etc. Since the wavelet transform provides information both in time and frequency, it is very helpful in our case to separate out the high-frequency TEC fluctuations due to varying ionospheric irregularities which we need in this analysis for deriving $\sigma^{w}_{\phi a}$. Apart from that, the wavelet transform also preserves the local features of the signal [*Starck et al.*, 1998; *Torrence and Compo*, 1998; *Materassi and Mitchell*, 2007] and this helps in reconstructing the signal after filtering for the estimation of true scintillation values compared to the HPF filters which result in misinterpretation of scintillation values if the cutoff frequency is increased [*Forte*, 2005, 2007]. The wavelet-filtered new analogous phase index $\sigma^{w}_{\phi a}$ can be given as

$$\sigma^{w}_{\phi a} = \left[\varpi\left(\chi\left(M\right), v_p\right) \times \sigma_{\mathrm{VTEC}'_{wav}}\right] \tag{12}$$

where $\sigma_{\mathrm{VTEC}'_{wav}}$ is the wavelet-filtered normalized standard deviation of the VTEC'_{wav} given in equation (13)

$$\sigma_{\mathrm{VTEC}'_{wav}} = \mathrm{std}\left[M\left\{\frac{\partial \mathrm{TEC}}{\partial x}v_p + \frac{\partial \mathrm{TEC}}{\partial t}\mathrm{d}t\right\} + \mathrm{TEC}\frac{\Delta M}{\Delta t}\right]_{wav} \tag{13}$$

where std is the normalized standard deviation of the $\sigma_{\mathrm{VTEC}'_{wav}}$ over 60 s after wavelet filtering.

2.1. Derivation of $\sigma_{\mathrm{VTEC}'_{wav}}$ Using Wavelet-Based Filtering

The wavelet transform can be defined as the multiplication of a signal $x(t)$ by the scaled and shifted versions of a mother wavelet $\psi(t)$ over a given time interval. Mathematically, the continuous wavelet transform (CWT) can be given as

$$c(s,\tau) = \frac{1}{\sqrt{s}}\int_{-\infty}^{\infty} x(t)\psi^*\left(\frac{t-\tau}{s}\right)\mathrm{d}t \tag{14}$$

where s is the scaling parameter used for stretching or compressing the signal, τ is the position parameter used for delaying the signal along the time axis, and $c(s,\tau)$ are the wavelet coefficients. The symbol $\psi^*(.)$ denotes the complex conjugation. In the CWT, the mother wavelet $\psi^*(.)$ acts as a window function the same as in the case of short-time Fourier transform (STFT), but, in the CWT, the window size is variable and depends on the scaling parameter s. In this analysis, we used the CWT for filtering the low-frequency TEC fluctuations in equation (13). However, the signal that we are using is a discrete time sequence, so in order to apply CWT on a discrete signal, we must use a discrete time version of the CWT. Suppose

$$x[n] = \left[M\left\{\frac{\partial \mathrm{TEC}}{\partial x}v_p + \frac{\partial \mathrm{TEC}}{\partial t}\mathrm{d}t\right\} + \mathrm{TEC}\frac{\Delta M}{\Delta t}\right] \tag{15}$$

The second term in equation (15), i.e., $\mathrm{TEC}\frac{\Delta M}{\Delta t}$, represents the very low-frequency TEC fluctuations and can be neglected. The wavelet filtering must be applied on $M(E)\left\{\frac{\partial \mathrm{TEC}}{\partial x}v_p + \frac{\partial \mathrm{TEC}}{\partial t}\mathrm{d}t\right\}$, as it represents the high-frequency TEC fluctuations. The CWT of $x[n]$ in discrete time can be given as

$$c_\tau[s] = \sum_{n=0}^{N-1} x[n]\psi^*\left[\frac{(n-\tau)}{s}\right] \tag{16}$$

where N is the total number of data points for wavelet analysis. The wavelet transform in equation (16) would result in wavelet coefficients $c_\tau[s]$ as a function of scale parameter s and position parameter τ. If we define

$$\psi_s[n] = \frac{1}{\sqrt{s}}\psi^*\left[\frac{-n}{s}\right]\mathrm{d}t \tag{17}$$

then equation (16) can be rewritten as

$$c_\tau[s] = \sum_{n=0}^{N-1} x[n]\psi_s[\tau - n] \tag{18}$$

Equation (18) shows that wavelet transform is a convolution of $x[n]$ with $\psi_s[\tau - n]$ where for every given scale parameter s, convolution is to be performed for each value of τ (position parameter). In this analysis, we used the Morlet wavelet as our mother wavelet whose mathematical form is given in equation (19).

$$\psi(t) = \pi^{-0.25} \exp\left(i\omega_0 t - \frac{1}{2}t^2\right) \tag{19}$$

The reason for choosing the Morlet wavelet is its good time and frequency resolution [*Torrence and Compo*, 1998] and its nonorthogonality which, when analyzing TEC data, can be used to represent the very high and low frequency TEC fluctuations. The wavelet transform can be efficiently computed in the frequency domain by taking the discrete Fourier transforms of $x[n]$ and $\psi_s[\tau - n]$. If we define $\hat{X}(.)$ as the Fourier transform (FT) of the input signal $x[n]$ and $\hat{\psi}(.)$ as the FT of the Morlet wavelet, then the CWT in Fourier domain can be given as

$$C_\tau(s) = \frac{1}{N}\sqrt{\frac{2\pi s}{\delta t}}\sum_{k=0}^{N-1}\hat{X}\left(\frac{2\pi k}{N\delta t}\right)\hat{\psi}^*\left(s.\frac{2\pi k}{N\delta t}\right)e^{j2\pi k\tau/N} \tag{20}$$

where δt is the sampling interval, $k = 0, 1, 2, ..., N-1$ is the frequency index, $\omega_k = \frac{2\pi k}{N\delta t}$ is the angular frequency, and $\sqrt{\frac{2\pi s}{\delta t}}$ is the normalization factor for the mother wavelet to have unit energy at every given scale parameter s. Equation (20) shows the wavelet transform as the inverse Fourier transform of the product of the Fourier transforms of $x[n]$ and $\psi[n]$. In frequency domain, the Morlet wavelet can be given as

$$\hat{\psi}(s\omega_k) = \pi^{-0.25}\exp\left(-\frac{(s\omega_k - \omega_0)^2}{2}\right) \tag{21}$$

In equation (21), the selection of the scale parameter s is the most important factor for time/frequency versus scales representation and also for signal reconstruction, once filtering is done. Although arbitrary values for the scale parameter can be used, the scales used in our analysis are based on the fractional powers of 2 [*Torrence and Compo*, 1998]:

$$s_j = s_0 2^{j\delta j}, j = 0, 1, ..., J \tag{22}$$

$$J = 2(\delta j^{-1}\log_2(N\delta t/s_0)) \tag{23}$$

where s_0 is the smallest scale ($s_0 = 2\delta t$) and δt is the sampling interval which is 1 s as we are using 1 Hz raw TEC data. J is the largest scale, δj is the scale increment factor for fine resolution, and N is the total number of data points. A large s means that a more stretched wavelet in the time domain is used for wavelet analysis, whereas a small s means that a more compressed wavelet is utilized. A graphical representation of the wavelet transform of $x[n]$ using 500 s long TEC 1 Hz data on 24 April 2012 at Trondheim (63.41°N, 10.4°E) is shown in Figure 1. For this graphical representation, we generated a Morlet wavelet of arbitrary window length starting at scale s_1. In Figure 1, we can see that as the scaling parameter s is increasing, the wavelet is stretching in time domain and achieving a fine frequency resolution compared to small scales which provide better time resolution due to compressed wavelets. The grey vertical lines in the figure represent how the wavelet is being stretch with the increasing scale value and the area of the signal $x[n]$ covered by the wavelet along the time axis for computing the wavelet coefficients $C_\tau(s)$. The complete wavelet transform will result in wavelet coefficients $C_\tau(s)$ for every possible value of the scale parameter s.

Once suitable values are selected for scale parameter s, filtering of the signal $x[n]$ can be done by reconstruction through the inverse wavelet transform (ICWT) of the wavelet coefficients ($C_\tau(s)$) in equation (24)

$$x_n = \left(\frac{\delta j \delta t^{0.5}}{C_\delta \psi_0(0)}\right)\sum_{j=j_1}^{j_2}\frac{Re(C_\tau(s_j))}{(s_j)^{0.5}} \tag{24}$$

In equation (24), x_n is the reconstructed signal after filtering, $C_\tau(s_j)$ are the wavelet coefficients, C_δ is a constant with a value of 0.776, $\psi_0(0)$ is a constant with a value of $\pi^{0.25}$, and j_1 and j_2 are the upper and lower boundary limits for the scale parameter s. The filtering of the signal $x[n]$ is achieved by discarding the scales which represent the low-frequency TEC fluctuations in equation (24). The selection of scales in equation (24) for performing wavelet filtering is discussed in the next section.

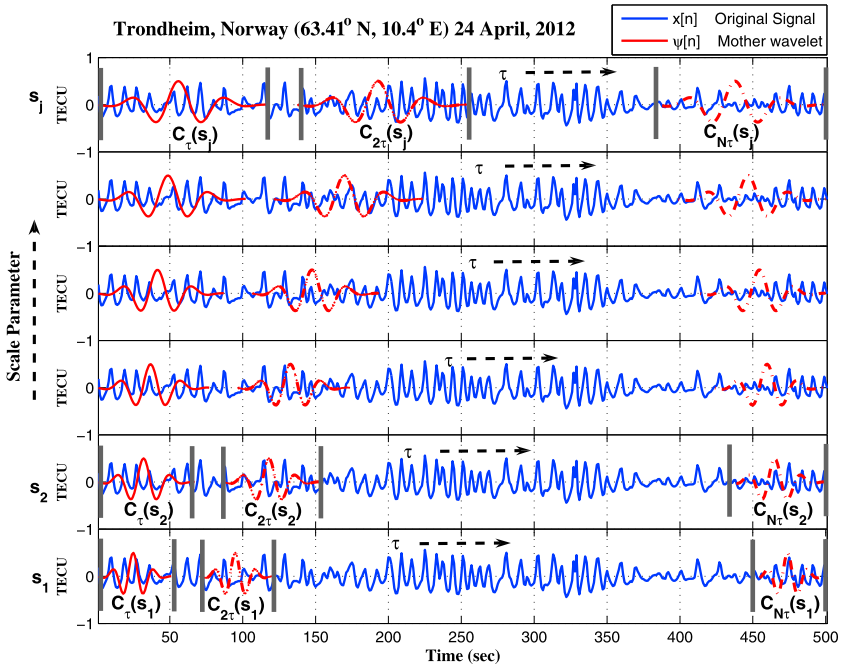

Figure 1. Graphical representation of the wavelet transform using the Morlet wavelet.

2.2. Experimental Setup and Selection of Scales for Wavelet-Based Filtering

In order to select suitable scale boundaries (j_1, j_2) in equation (24) for filtering the signal $x[n]$, we calculated the wavelet coefficients of the signal through the Fourier transform using equation (20). These wavelet coefficients were then used to construct the scalograms of the signal to show the wavelet statistical energy $E(s,\tau) = \mid C_\tau(s) \mid^2$ associated with the high- and low-frequency TEC fluctuations. For the calculation of wavelet coefficients in equation (20), the following values are used: $\delta t = 1$, $s_0 = 2\delta t$, $\delta j = 0.125$, and J is calculated from equation (20) which actually depends on the total number of data points used.

The data used for the scalogram generation was collected using a NovAtel GISTM GSV 4004B dual-frequency GPS receiver installed at Trondheim, Norway (63.41°N, 10.4°E). Two types of data were logged using the GISTM GPS receiver: data at 50 Hz used to estimate the amplitude and phase scintillation index (S_4, σ_ϕ) and 1 Hz raw TEC data used in scalogram generation and the estimation of $\sigma_{\phi a}$ and $\sigma^{w}_{\phi a}$. Apart from this, the *H* and *Z* components of the Earth's magnetic field from Dombas (62.07°N, 9.11°E) close to Trondheim were used in order to measure the local geomagnetic activity associated with the storm.

The scalograms of 2 days for selected pseudo-random number based on different geomagnetic conditions ($Kp \leq 5$, $Kp \geq 6$) are shown in Figures 2 and 3. The reason for choosing different *Kp* values for the scalograms is to show the wavelet energy associated with the high- and low-frequency TEC fluctuations during different geomagnetic conditions, i.e., no geomagnetic storm/minor storm ($Kp \leq 5$) and strong geomagnetic storm ($Kp > 5$).

For $Kp \leq 5$ case, the scalograms of the TEC fluctuations on 26 April 2012 are shown in Figures 2a–2i for the PRNs that were visible between 00:00 and 06:00 UT. The *Kp* plot is shown in Figure 2j where it is found that in the early hours of the day, there was a minor geomagnetic storm from 03:00 to 06:00 UT (shown by a red bar) preceded by a geomagnetic disturbance from 00:00 to 03:00 (shown by a yellow bar). The green bars show the no-storm case. In order to further confirm the effect of geomagnetic disturbance locally at Trondheim (63.41°N, 10.4°E), we also plotted the *H* component of the Earth magnetic field at Dombass (62.07°N, 09.11°E) close to Trondheim. The local variations in the Earth magnetic field also confirmed the disturbed ionosphere between 02:00 and 04:00 UT. When plotting the scalograms, the largest scale *J* is calculated based on the length of the data points using equation (23). For example, in Figure 2g, PRN 19 was visible for 5 h (00:00 to 05:00 UT). The total number of data points were found to be 17,260 when the satellite was visible and locked.

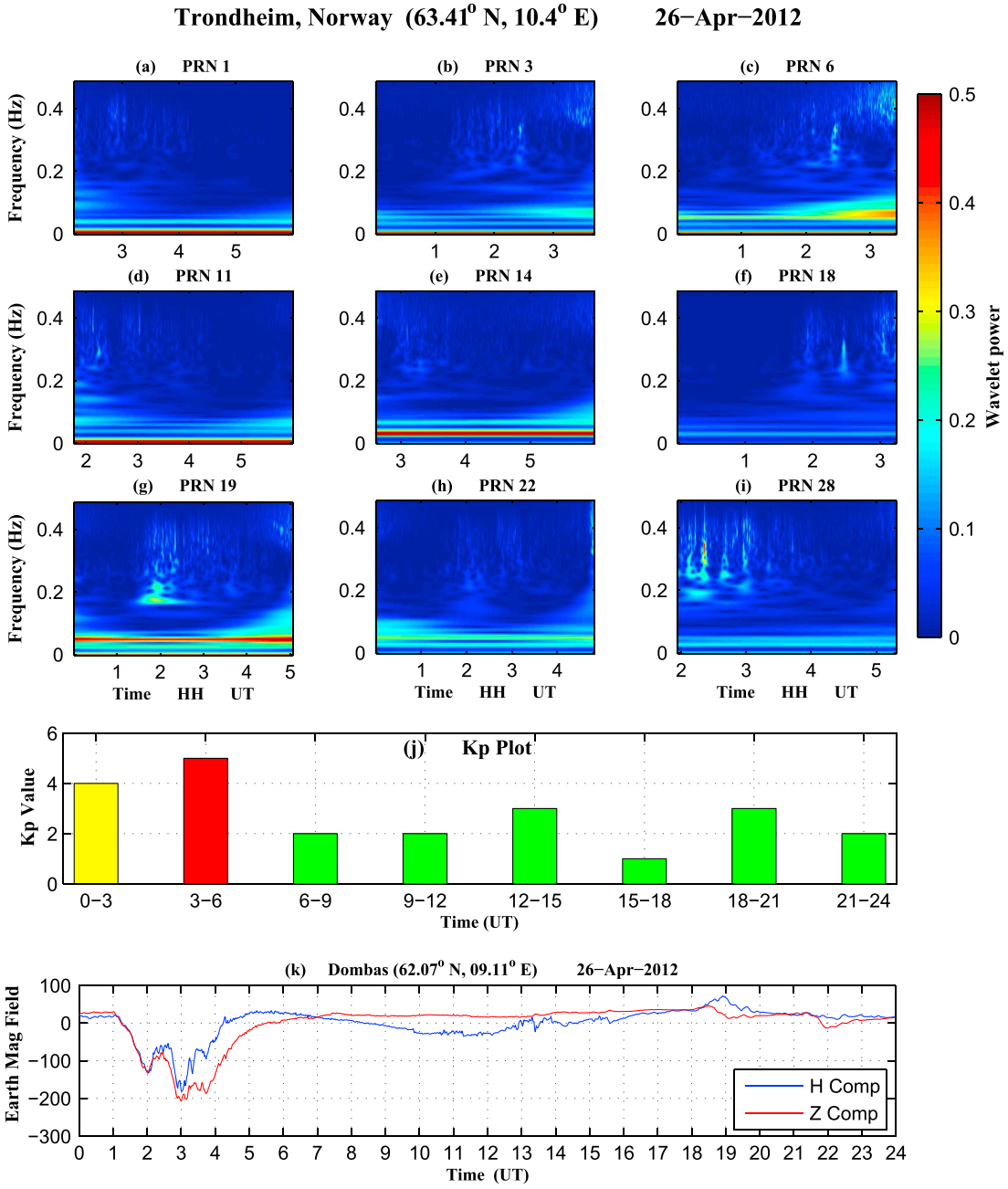

Figure 2. Scalograms and the geomagnetic field plots for different PRNs on 26 April 2012 when $Kp \leq 5$.

In this case, the largest-scale J was calculated as 208 using equation (23) for the 5 h (00:00 to 05:00 UT) of data. The scales are then converted to their equivalent frequencies using equation (25).

$$\text{frequency} = \frac{6 + \sqrt{2 + 6^2}}{4\pi \times \text{scales}} \tag{25}$$

In Figures 2a–2i, most of the power resides in the large scales/small frequencies (scales > 7s ∼(frequencies < 0.15 Hz)), depicting low-frequency TEC fluctuations which are due to satellite-receiver motion, Doppler shift and slowly varying background ionosphere, and need to be eliminated. However, some medium- to high-power TEC fluctuations were also observed for PRNs 6, 19, and 28 for small scales/high frequencies (scales < 6s ∼ (frequencies > 0.16Hz)) representing scintillation signatures for these PRNs between 02:00

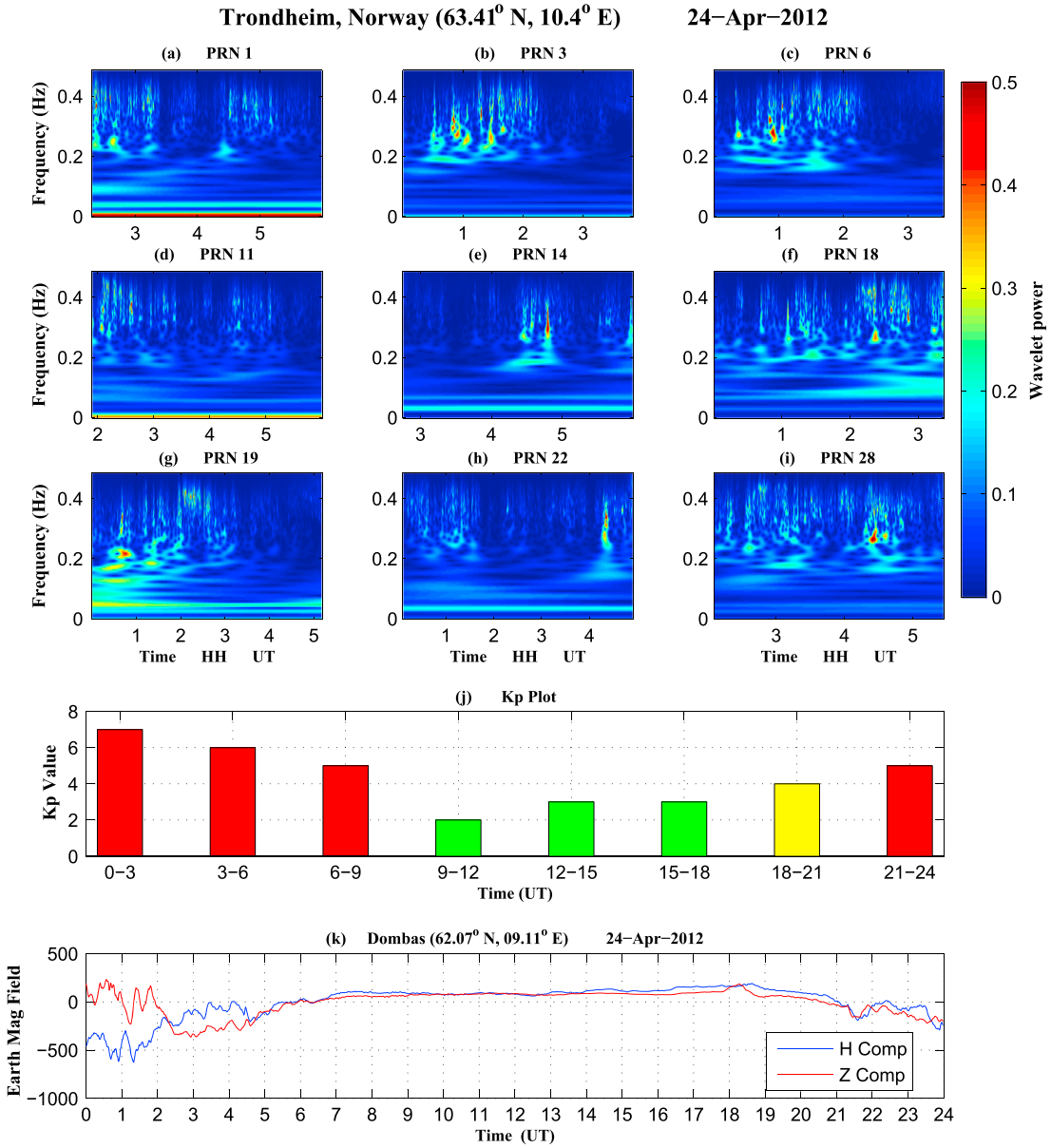

Figure 3. Scalograms and the geomagnetic field plots for different PRNs on 24 April 2012 when $Kp \geq 6$.

and 04:00 UT due to the effect of a local minor storm. This also confirms that the wavelet transform can be used as an efficient tool for representing a true picture of scintillation signatures.

For $Kp > 6$ case, scalograms of the PRNs visible between 00:00 and 06:00 on 24 April 2012 are plotted in Figures 3a–3i when there was a severe geomagnetic storm. The *Kp* and the geomagnetic field plots for the day are shown in Figures 3j and 3k, respectively. A strong variation in the *H* and *Z* components of the geomagentic field at Dombas shows the local effect of the storm. If we look at the scalograms of the PRNs in Figures 3a–3i, we observe that all the PRNs are affected by the storm at different times between 00:00 and 06:00 UT as we can clearly see high-power TEC fluctuations (red and yellow spots) for small scales/high frequencies (scales $< 7s \sim$ (frequencies > 0.14 Hz)) depicting strong scintillation. PRNs 18, 19, and 28 are those which are highly affected during this time. In order to elaborate this further, let us consider the scalogram of PRN 19 in Figure 3g. Medium- to high-power TEC fluctuations are observed for this PRN from 00:00 to 03:00 UT for small scales (scales $< 6s \sim$ (frequencies > 0.15 Hz)) and hence resulted in high phase scintillation values. Also, there are low-frequency TEC fluctuations for large scales/small frequencies (scales $> 7s \sim$ (frequencies > 0.15Hz))

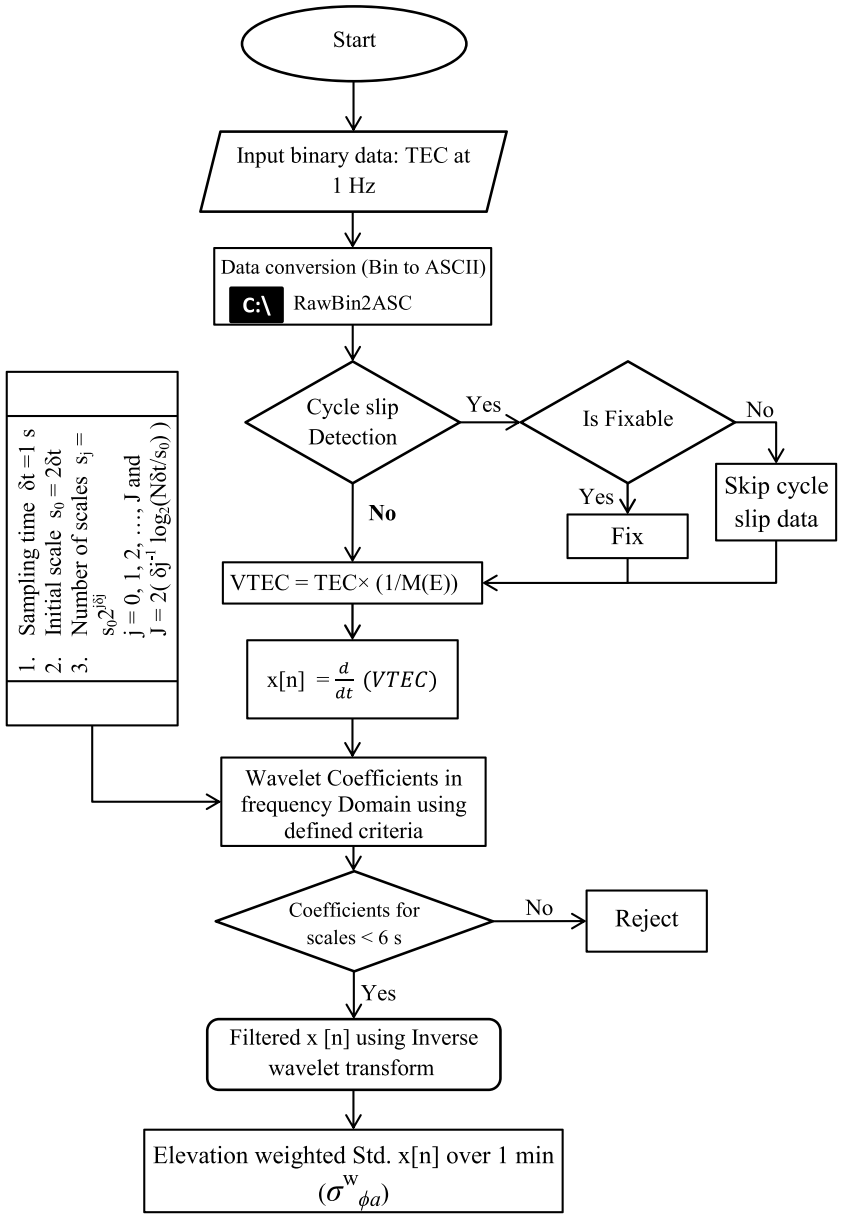

Figure 4. Flowchart for $\sigma^{w}_{\phi a}$ using raw TEC 1 Hz data.

which must be removed for data filtering to consider only those TEC variations which are related to high frequencies and represent scintillation signatures.

Based on the discussion above and after carefully observing the scalograms of the scintillation events between August 2011 and September 2012, we removed the large scales (scales > 6s(frequencies < 0.15Hz)) and used only the small scales (scales < 6s ~ (frequencies > 0.15 Hz)) in equation (24), which represent the high-frequency TEC fluctuations due to ionospheric irregularities.

A flowchart of the complete process of deriving $\sigma^{w}_{\phi a}$ from data collection to obtaining $\sigma^{w}_{\phi a}$ is shown in Figure 4. The process actually starts by collecting raw GPS data in binary format which is then converted to ASCII. The ASCII data are then checked for cycle slips. If cycle slips are found, then the program will try to fix them. If the cycle slips are not fixed, then the program will start from the beginning by taking the next data set. If cycle slips are fixed or if there are no cycle slips, then VTEC will be computed which will then be used to compute the $x[n]$ which needs to be filtered to remove the low-frequency TEC fluctuations. After applying the wavelet transform and rejecting the selected scales as mentioned in Figure 4, the inverse wavelet transform is taken

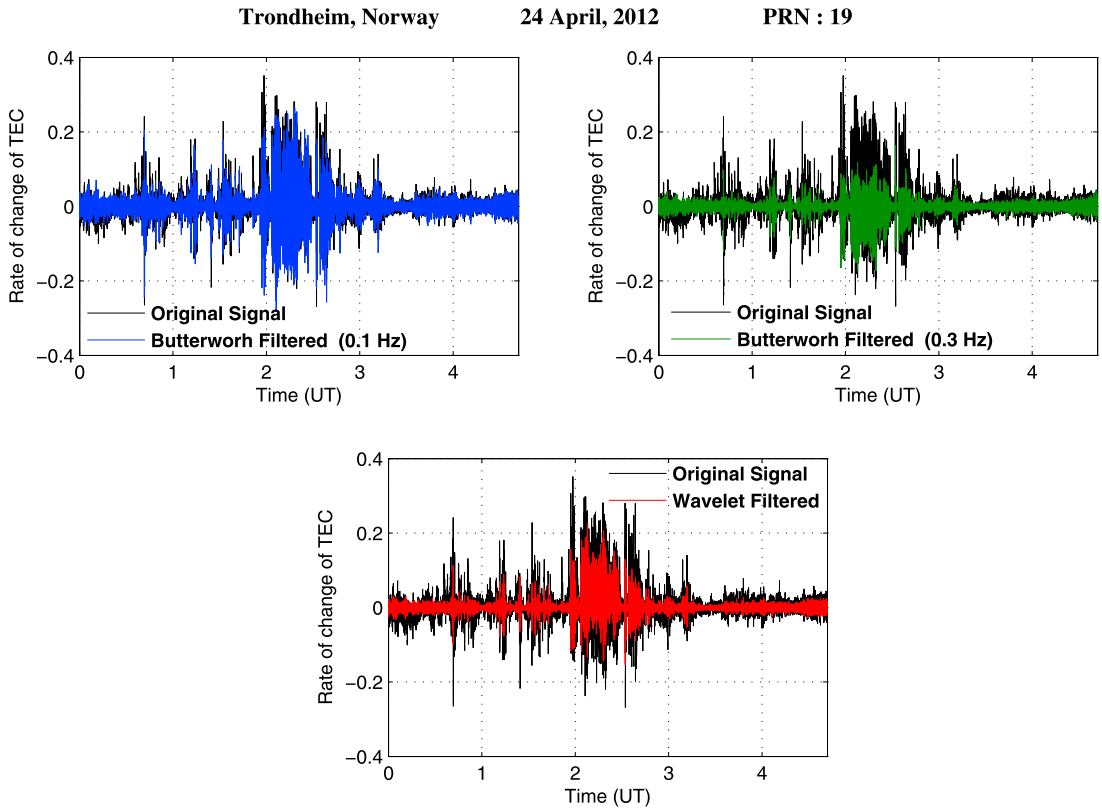

Figure 5. Filtering the low-frequency TEC fluctuations using the wavelet transform and Butterworth filter with different cutoff frequencies for PRN 19.

to get the $x[n]$. The standard deviation (std) over 60 s will then be taken to generate the values for the $\sigma_{\phi a}^{w}$ which is then multiplied by the elevation weighting function $\varpi\left(\chi\left(M\right), v_p\right)$.

Figure 5 shows the effects of filtering on the time derivative of TEC (ROT) in removing the low-frequency TEC fluctuations when a Butterworth filter with different cutoff frequencies was applied and was then compared with the wavelet filtering. The data used in Figure 5 were for PRN 19 on 24 April 2012 when there was a strong geomagnetic storm from 00:00 to 06:00 UT and for which high scintillation values were recorded during this time. In Figure 5, Butterworth filtering with a 0.1 Hz cutoff frequency shows no effects on the original signal, and we can still see the slower trends which are not fully removed. *Forte* [2005] also mentioned that using the low cutoff frequency of 0.1 Hz will result in misleading information especially at high latitudes when there is weak to moderate scintillation as the filter may not be able to separate the diffractive effects from the refractive effects since diffractive effects are the main cause of scintillation due to small-scale irregularities at high latitudes. On the other hand, increasing the cutoff frequency to 0.3 Hz has somewhat removed the slower trends but has also removed the useful information which resulted in transforming the high scintillation event to medium scintillation event as shown in Figure 6. It was also mentioned by *Forte* [2005] that increasing the cutoff frequency while estimating the phase scintillation may reduce the intensity of scintillation which can turn the high scintillation to moderate scintillation levels which we also observed in Figure 6 when we increased the cutoff frequency to 0.3 Hz when estimating the scintillation values. It can be seen in Figure 5 that filtering of the low-frequency TEC fluctuations using the wavelet transform has not only removed the slower trends but also saved the useful information. The scintillation estimation of the three indices based on the filtering effects are shown in Figure 6 for PRN 19 in the next section.

3. Performance Comparison Between $\sigma_{\phi a}^{w}$, $\sigma_{\phi a}$, and σ_{ϕ}

In this section, the performance of the $\sigma_{\phi a}^{w}$ with $\sigma_{\phi a}$ and with σ_{ϕ} is compared by estimating the scintillation values for a whole 1 year of data from October 2011 to September 2012. The comparison is first made for PRN 19 where the difference between $\sigma_{\phi a}^{w}$ and $\sigma_{\phi a}$ is shown based on filtering and is then compared with the σ_{ϕ}. A good correlation was found between the three indices apart from after 02:30 UT when we saw some

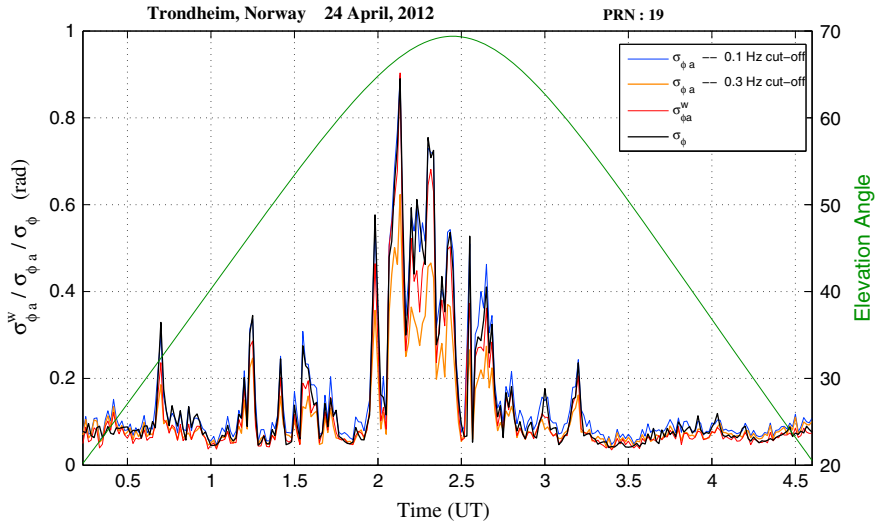

Figure 6. The $\sigma^{w}_{\phi a}$ with $\sigma_{\phi a}$ and σ_{ϕ} for PRN 19 on 24 April 2012.

small overestimation factor in case of $\sigma_{\phi a}$. On the other hand, $\sigma_{\phi a}$ estimated using the 0.3 Hz cutoff has reduced the intensity of scintillation to moderate level as discussed above. The comparison is then made for the rest of the PRNs that were visible between 00:00 and 08:00 UT on 24 April 2012 in order to give a clearer view of the comparative correlation and scintillation intensities using the actual $\sigma^{w}_{\phi a}$, $\sigma_{\phi a}$, and σ_{ϕ}.

In Figure 7, after comparing the results of all the PRNs on 24 April 2012, we observed that the TEC-derived indices ($\sigma^{w}_{\phi a}$, $\sigma_{\phi a}$) are better estimating the scintillation values by taking into account the effect of both the background noise and the elevation angle compared to the conventional scintillation index σ_{ϕ}. In Figure 7, it is observed that there is a good correlation between the three indices when the elevation angle is higher than 30°. However, when the elevation angle drops below 30°, the overestimated scintillation values in case of σ_{ϕ} becomes intolerable especially in the cases of PRNs 7, 8, 17, 18, 21, 28, and 31 which definitely points to the fact that σ_{ϕ} is unable to distinguish between the actual scintillation and the background noise. It was also mentioned by *Forte* [2005] that the σ_{ϕ} index cannot distinguish between the actual scintillation and the background noise at low elevation angles and during weak to moderate scintillation conditions.

For the TEC-derived indices, we also observed some unexpected high scintillation values in the case of PRNs 10, 13, and 23 for a short period of time in the beginning when the receiver was in lock state. It should be noted that the TEC-derived indices have a sampling rate of 1 Hz and use the dual-frequency observations compared to σ_{ϕ} which operates at 50 Hz sampling rate, uses single-frequency observations, and has a very fast converging rate, i.e., 20 ms. Thus, the TEC-derived indices and σ_{ϕ} behave differently during the lock phase and may have some errors in the beginning which can be discarded. In case of PRNs 10, 13, and 23, the receiver is in lock phase in the beginning and, due to a slow convergence rate along with other factors, gives a few (approximately 7 to 8) high scintillation values. The example taken in Figure 7 is for a single day when $Kp \geq 5$; although the reduction in the overestimated scintillation values using $\sigma^{w}_{\phi a}$ does not seem to be too appreciable, this analysis is extended in Figures 10 and 11 by plotting all the scintillation values for one whole year of data. The sky view plot of $\sigma^{w}_{\phi a}$, $\sigma_{\phi a}$, and σ_{ϕ} with respect to both the elevation and azimuth angle are shown in Figure 8 for the PRNs shown in Figure 7.

The number of occurrences of $\sigma^{w}_{\phi a}$, $\sigma_{\phi a}$, and σ_{ϕ} are further calculated in Figure 9 for a complete 1 year data from October 2011 to September 2012 for $Kp > 4$ to show the daytime and nighttime scintillation activity using the magnetic local time (MLT) at Trondheim, Norway. It was also mentioned by *Prikryl et al.* [2014] that the scintillation activity is strongly associated with the MLT and, at high latitudes, is dominant during the nighttime due to the coupling between the solar wind, the magnetosphere, and the ionosphere. The probabilistic forecasting of phase scintillation was also presented by *Prikryl et al.* [2012] based on the arrival times, i.e., corotating interaction regions and interplanetary coronal mass ejections. In this analysis, only those events are considered where the scintillation values are greater than 0.3 to reflect a complete picture of scintillation activity during a weak to strong storm. In Figure 9, the number of occurrences are high between 20:00 and 07:00 MLT

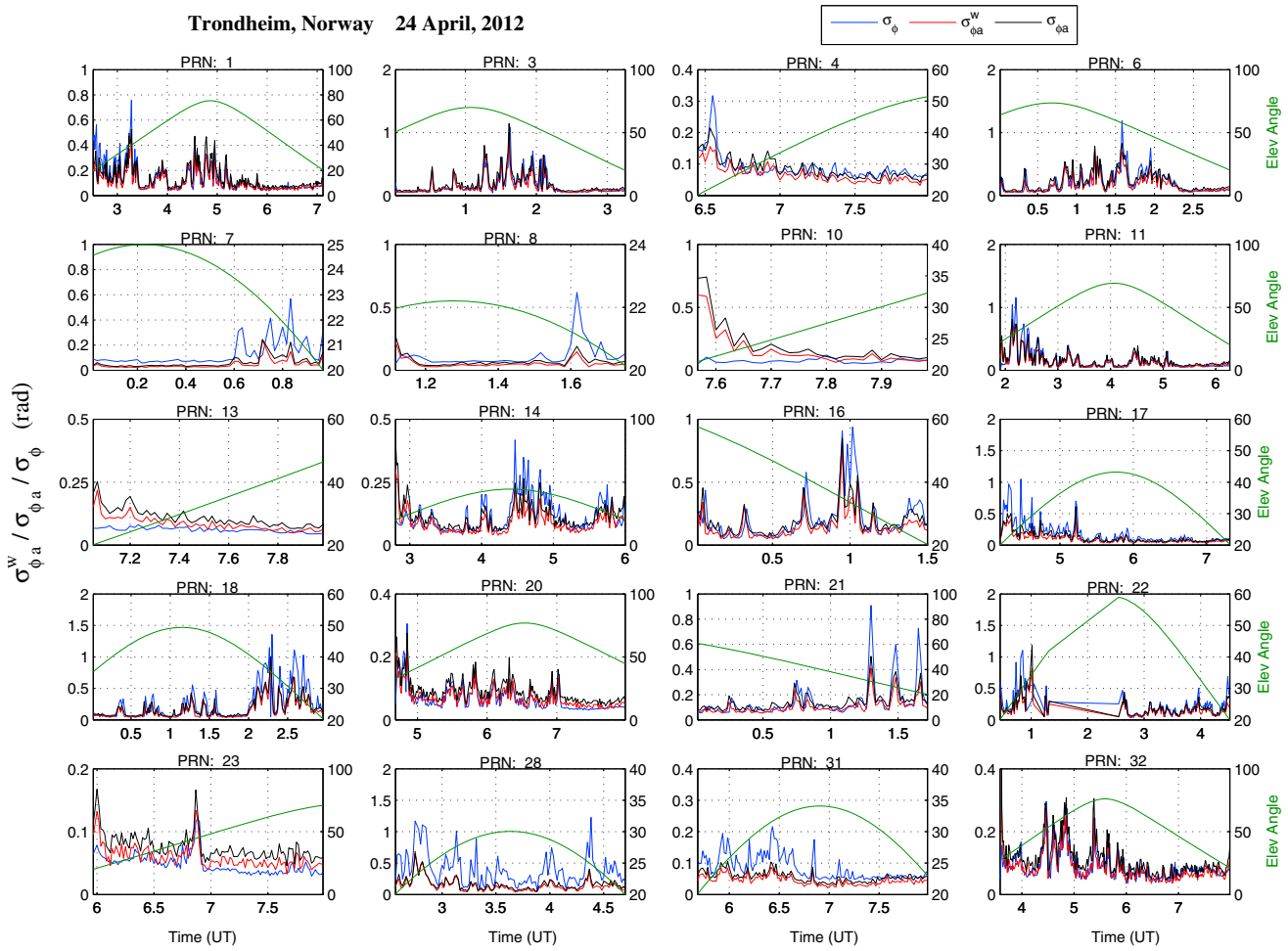

Figure 7. The $\sigma^{w}_{\phi a}$, $\sigma_{\phi a}$, and σ_{ϕ} comparison for all the visible satellites between 00:00 and 08:00 UT on 24 April 2012.

(premidnight and postmidnight) due to auroral activity resulting in high phase scintillation values as a result of ionospheric irregularities at high latitudes [*Aarons et al.*, 2000; *Prikryl et al.*, 2014]. It is also indicated by *Basu et al.* [1998] and *Aarons et al.* [2000] that due to *F* region blobs during a geomagnetic storm, the phase varies within ±3 TECU (total electron content unit, 1 TECU = 10^{16} el m^{-2}) and hence results in high scintillation values.

In Figures 10 and 11, the scintillation values between the $\sigma^{w}_{\phi a}$ and $\sigma_{\phi a}$ and between $\sigma^{w}_{\phi a}$ and σ_{ϕ} are plotted for two different geomagnetic conditions ($Kp < 5$; $Kp \geq 5$) by recording the data at Trondheim, Norway for a whole 1 year from October 2011 to September 2012. Furthermore, the comparison is made by dividing the data into four seasons to observe the seasonal variations in the scintillation occurrence pattern as well. Due to Trondheim being located at a high northern latitude, the seasons are defined as follows: autumn (21 September to 20 December), winter (21 December to 20 March), spring ((21 March to 20 June), and summer (21 June to 20 September). The corresponding correlation between the indices in each case is also determined by calculating the Pearson's correlation coefficient *R* [*Cleff*, 2009]. The *Kp* values are averaged every 3 h, so in 24 h there are eight *Kp* values divided into 3 h time slots. It should be noted that in Figures 10 and 11, while plotting the scintillation values for $\sigma^{w}_{\phi a}$, $\sigma_{\phi a}$, and σ_{ϕ}, only those 3 h time slots are used where the *Kp* value was either greater than or equal to 5 (Figure 10) or less than 5 (Figure 11). In addition to this, minimum elevation angle cutoff of 20° was used in order to make sure that the elevation angle effect is minimal when estimating the scintillation values using the above indices.

For the $Kp \geq 5$ case, Figure 10a shows the scintillation values for the $\sigma^{w}_{\phi a}$ and $\sigma_{\phi a}$, whereas Figure 10b contain the scintillation values for the $\sigma^{w}_{\phi a}$ and σ_{ϕ} for all the four seasons. A very good correlation was found between the $\sigma^{w}_{\phi a}$ and $\sigma_{\phi a}$ in all cases (Figure 10a) with an average correlation coefficient of approximately 0.92. The

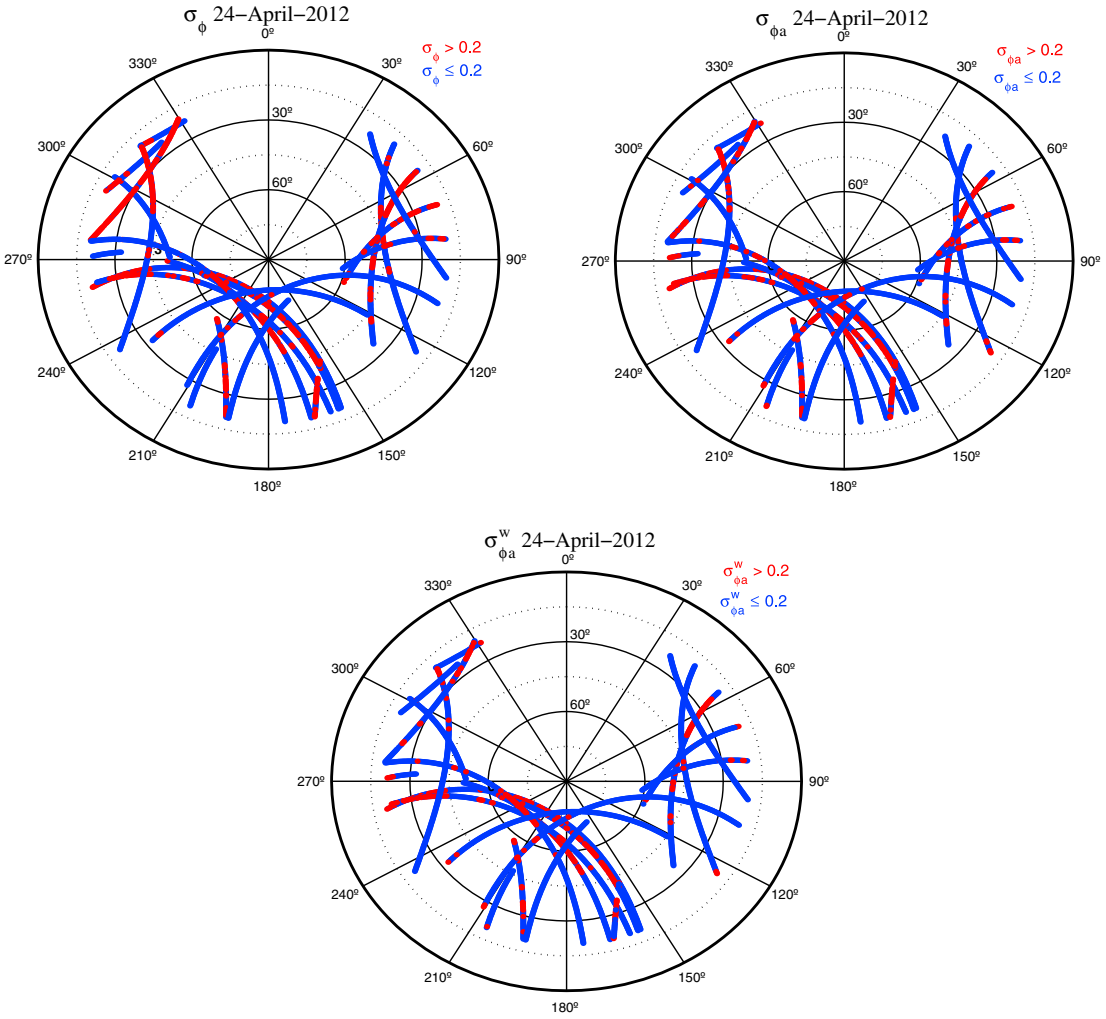

Figure 8. Sky view of the phase scintillation for all the visible PRNs between 00:00 and 08:00 UT on 24 April 2012 at Trondheim, Norway.

scintillation occurrence patterns of $\sigma^{w}_{\phi a}$ and $\sigma_{\phi a}$ were also quite similar, and no unexpected differences in the scintillation patterns were observed for the $Kp \geq 5$ case. On the other hand, the scintillation values comparison between the $\sigma^{w}_{\phi a}$ and σ_{ϕ} in Figure 10b also showed a good correlation in all the four seasons with an average correlation coefficient of 0.78, although it is still lower than the average correlation coefficient that exists between the $\sigma^{w}_{\phi a}$ and $\sigma_{\phi a}$ values. This is due to the overestimated scintillation values in the case of σ_{ϕ}, although both the $\sigma^{w}_{\phi a}$ and σ_{ϕ} values follow a very similar occurrence pattern (Figure 10b) in all seasons. As discussed earlier, the high scintillation values in the case of σ_{ϕ} could be most likely due to the selection of an inappropriate cutoff frequency in the detrending process which, at low elevation angles during strong scintillation conditions, results in high scintillation values as discussed by many researchers [*Forte*, 2005, 2007; *Mushini et al.*, 2012]. Apart from the existence of a fairly good amount of correlation between the $\sigma^{w}_{\phi a}$ and σ_{ϕ} values and also between those of $\sigma^{w}_{\phi a}$ and $\sigma_{\phi a}$, the similarity in the scintillation occurrence patterns shows that the $\sigma^{w}_{\phi a}$ is a very useful index to represent the phase scintillation activity at European high latitudes during strong scintillation conditions. It should be noted that some of the previously proposed indices using the wavelet transform [*Mushini et al.*, 2012; *Niu et al.*, 2012] are only tested for weak scintillation conditions with a very limited data set.

For the $Kp < 5$ case, the scintillation values for the $\sigma^{w}_{\phi a}$ and $\sigma_{\phi a}$ are plotted in Figure 11a whereas Figure 11b contain the scintillation values of $\sigma^{w}_{\phi a}$ and σ_{ϕ} for the four previously defined seasons. On average, a correlation coefficient of 0.86 was found between the $\sigma^{w}_{\phi a}$ and $\sigma_{\phi a}$ (Figure 11a) due to the similarity in the scintillation occurrence pattern and also due to the fact that both the $\sigma^{w}_{\phi a}$ and $\sigma_{\phi a}$ were derived from the same source where $\sigma^{w}_{\phi a}$ gives a better estimate of the scintillation values by removing the discrepancies involved in $\sigma_{\phi a}$

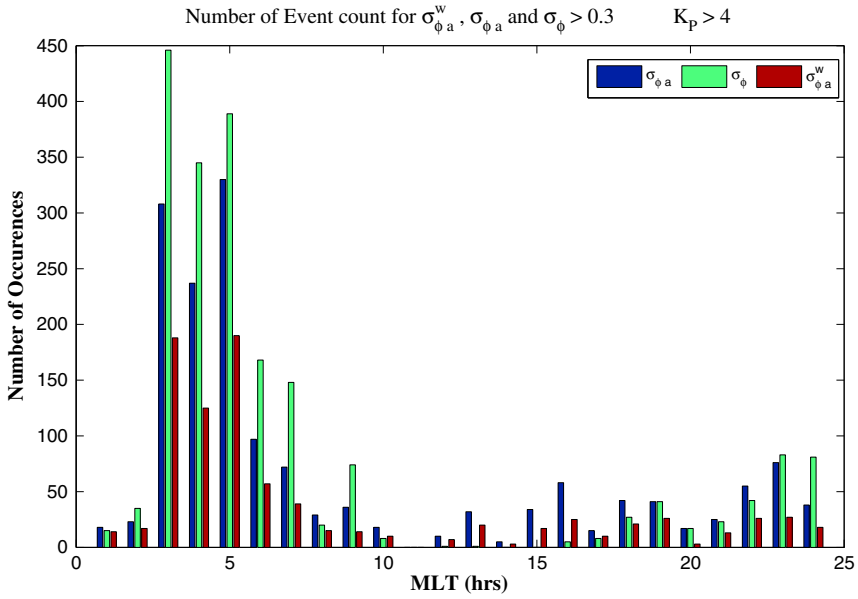

Figure 9. Number of occurrences of scintillation events for $\sigma^{w}_{\phi a}$, $\sigma_{\phi a}$, and σ_{ϕ} for all the satellites from October 2011 to September 2012.

estimation. However, the scintillation intensity and the number of scintillation events greater than 0.3 in the case of $\sigma_{\phi a}$ were much higher compared to both the $\sigma^{w}_{\phi a}$ and σ_{ϕ}. In *Tiwari et al.* [2013], an average correlation factor of 35% was found between the σ_{ϕ} and $\sigma_{\phi a}$ for weak scintillation conditions ($Kp < 5$). The point to be noted here is that in *Tiwari et al.* [2013], only those scintillation values were used for correlation which were greater than 0.2 and the reason behind the poor correlation may be the fact that the indices were derived from different data sources and with different sampling rates resulting in the possibility that the filtering effect using the digital filters could be quite different for $\sigma_{\phi a}$ compared to σ_{ϕ}. On the other hand, when $\sigma^{w}_{\phi a}$ was compared and correlated with σ_{ϕ} in Figure 11b for all the four seasons, an average correlation coefficient of 0.70 was found between the two indices. However, at certain times in Figure 11b in all the four seasons, the σ_{ϕ}

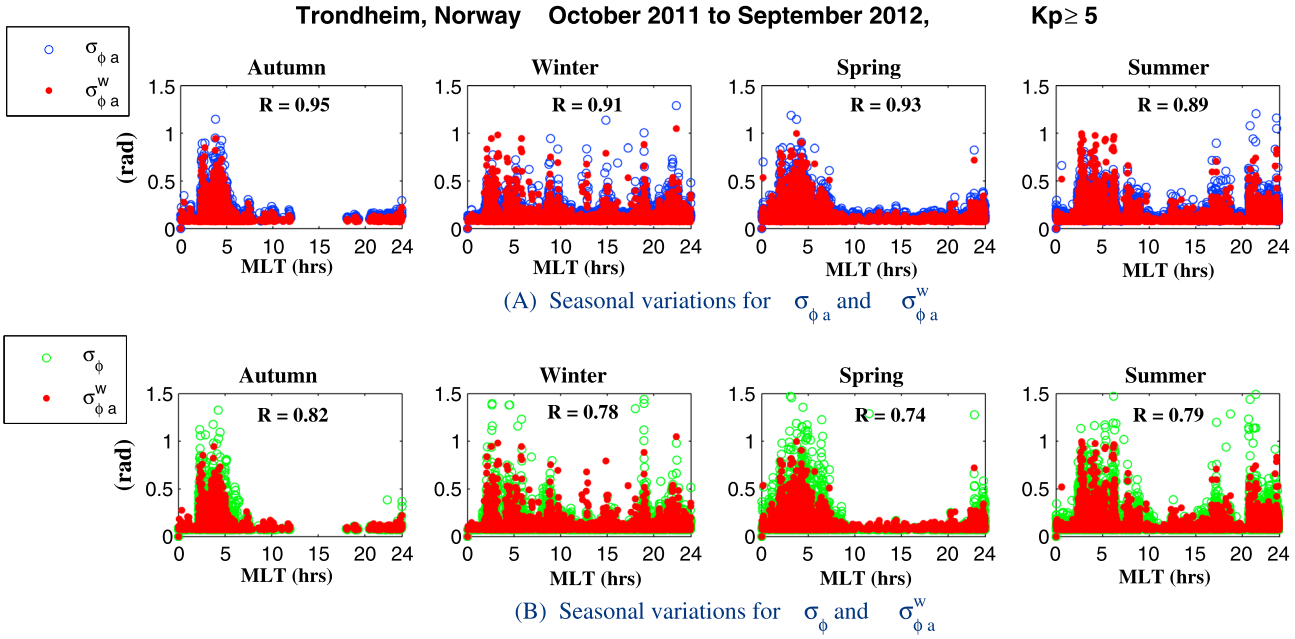

Figure 10. Seasonal variations of the scintillation occurrence patterns of $\sigma^{w}_{\phi a}$, $\sigma_{\phi a}$, and σ_{ϕ} for $Kp \geq 5$ case for a whole year from October 2011 to September 2012.

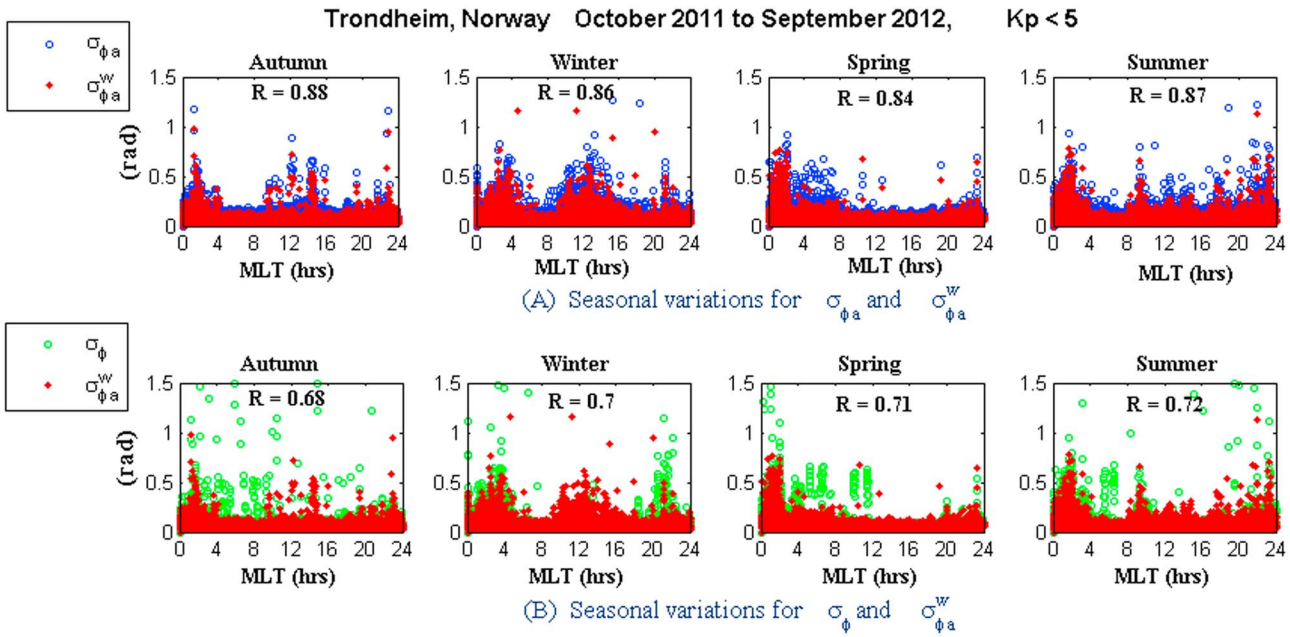

Figure 11. Seasonal variations of the scintillation occurrence patterns of $\sigma^{w}_{\phi a}$, $\sigma_{\phi a}$, and σ_{ϕ} for $Kp < 5$ case for a whole year from October 2011 to September 2012.

index possesses some very high values having an inconsistent pattern especially during the autumn, spring, and summer that does not match with $\sigma^{w}_{\phi a}$. These values of σ_{ϕ} cannot be considered as the true representative of the scintillation activity as *Kp* is less than 5 which can only result in scintillation activity of medium intensity at times when *Kp* is equals to 4. The $\sigma^{w}_{\phi a}$ values truly reflect the true representation of the scintillation activity based on the *Kp* index both for $Kp < 5$ and $Kp \geq 5$ cases. It was also mentioned by *Forte* [2005, 2007] that σ_{ϕ} is not a good indicator to distinguish between the actual scintillation and the background noise for weak to moderate scintillation conditions as, during these conditions, inappropriate filtering along with other additional factors led to high σ_{ϕ} values, especially at low elevation angles, even when there is no actual scintillation present. It was also observed that during the winter season, the behavior of the $\sigma^{w}_{\phi a}$ and σ_{ϕ} indices (Figure 11b) was different during the prenoon and postnoon sessions (09:00–15:00 MLT) where the $\sigma^{w}_{\phi a}$ was consistently giving some medium-intensity scintillation values between 0.3 and 0.7, whereas σ_{ϕ} reported low values during the same time. A further investigation revealed that on 7–9 March 2012, there occurred a strong geomagnetic storm with *Kp* as high as 7 during the prenoon and postnoon sessions. However, there were certain time slots where *Kp* was less than 5 but there was still a strong geomagnetic disturbance which resulted in scintillation of medium intensity for both the $\sigma^{w}_{\phi a}$ and $\sigma_{\phi a}$. At the same time, there were no scintillation values available from the NovAtel receiver for the σ_{ϕ} index. This can be due to the frequent loss of lock of low-elevation PRNs which may be forcing the GISTM receiver into reacquisition at short intervals of time. During these situations, the GISTM receiver uses the lock time as a filter and rejects 240–300 s of data to avoid spurious values, and this results in losing five to six scintillation values in the event of a loss of phase lock. On the other hand, for the estimation of the $\sigma^{w}_{\phi a}$ index, the cycle slip is fixed before estimating the scintillation values as shown in the flowchart in Figure 4, and hence less scintillation values are lost compared to the σ_{ϕ} index.

In order to further determine the statistical significance of the Pearson's correlation coefficient, *R*, between the $\sigma^{w}_{\phi a}$ and $\sigma_{\phi a}$ and also between the $\sigma^{w}_{\phi a}$ and σ_{ϕ}, a population correlation coefficient, i.e., the *p* value [*Cleff*, 2009] is computed by setting a significance level of $\alpha = 0.01$ for both the $Kp \geq 5$ and $Kp < 5$ cases in all the four seasons as defined in Figures 10 and 11. The *p* value defines the probability of getting a correlation as large as the observed value by a random chance. The results of the *p* value based on the sample sizes are shown in the tables in Figure 12 where *N* denotes the sample size and the significance level highlights whether the *p* value is less than 0.01 or not. For $Kp \geq 5$ case, Figure 12a1 shows the correlation significance test between the $\sigma^{w}_{\phi a}$ and $\sigma_{\phi a}$, whereas Figure 12a2 shows the correlation significance between the $\sigma^{w}_{\phi a}$ and σ_{ϕ}. Similarly, for $Kp < 5$ case, Figure 12b1 shows the correlation significance between the $\sigma^{w}_{\phi a}$ and $\sigma_{\phi a}$, whereas Figure 12b2 shows the correlation significance between the $\sigma^{w}_{\phi a}$ and σ_{ϕ}. In all the four seasons in both cases, i.e., $Kp \geq 5$ and

(1) $\sigma_{\phi a}{}^{w}$ and $\sigma_{\phi a}$

Autumn		Winter		Spring		Summer	
R	0.95	R	0.91	R	0.93	R	0.89
N	292,052	N	241,128	N	269,782	N	316,129
Significance level	p< 0.01	Significance level	p< 0.01	Significance level	p< 0.01	Significance level	p< 0.01

(2) $\sigma_{\phi a}{}^{w}$ and σ_{ϕ}

Autumn		Winter		Spring		Summer	
R	0.82	R	0.78	R	0.74	R	0.79
N	292,052	N	241,128	N	269,782	N	316,129
Significance level	p< 0.01	Significance level	p< 0.01	Significance level	p< 0.01	Significance level	p< 0.01

(a) Significance of the correlation coefficient R using 1 % significance level for $Kp \geq 5$ case

(1) $\sigma_{\phi a}{}^{w}$ and $\sigma_{\phi a}$

Autumn		Winter		Spring		Summer	
R	0.88	R	0.86	R	0.84	R	0.87
N	9,142	N	22,758	N	19,659	N	24,111
Significance level	p< 0.01	Significance level	p< 0.01	Significance level	p< 0.01	Significance level	p< 0.01

(2) $\sigma_{\phi a}{}^{w}$ and σ_{ϕ}

Autumn		Winter		Spring		Summer	
R	0.68	R	0.7	R	0.71	R	0.72
N	9,142	N	22,758	N	19,659	N	24,111
Significance level	p< 0.01	Significance level	p< 0.01	Significance level	p< 0.01	Significance level	p< 0.01

(b) Significance of the correlation coefficient R using 1 % significance level for $Kp < 5$ case

Figure 12. Statistical significance of the Pearson's correlation coefficient (R) between the $\sigma_{\phi a}^{w}$ and σ_{ϕ} and between the $\sigma_{\phi a}^{w}$ and $\sigma_{\phi a}$ using 1% significance level.

$Kp < 5$, the p value was found to be even less than 0.00001. If we consider the R values for the $Kp \geq 5$ and $Kp < 5$ cases, which falls between 0.68 and 0.96, we can say that the correlation of the $\sigma_{\phi a}^{w}$ index with both the $\sigma_{\phi a}$ and σ_{ϕ} indices is highly significant at the 0.01 level. Based on the significance test, we can also reject the null hypothesis, H_0, which states that there is no linear correlation against the alternative hypothesis, H_1, that there is a correlation [*Cleff*, 2009]. Hence, we can say that there is a strong linear correlation between the $\sigma_{\phi a}^{w}$ and σ_{ϕ} and also between the $\sigma_{\phi a}^{w}$ and $\sigma_{\phi a}$.

Although several researchers such as *Mushini et al.* [2012] and *Niu et al.* [2012] have reported the problem of filtering and used the wavelet transform, the analyses presented in those papers are limited and done only for a very short period of time (few minutes/hours), for weak scintillation conditions only and without considering any varying geomagnetic conditions which could verify that the methods used by them are a better estimate of the scintillation values. The $\sigma_{\phi a}^{w}$ show that the overestimation factor can be reduced to a fairly low level which can obviously help in estimating more accurate scintillation values. The main reason for proposing $\sigma_{\phi a}^{w}$ was to use this index in GPS tracking loop so that the large tracking error variances due to the overestimation factor can be reduced to a fairly low level, improving the performance of a GPS receiver during scintillation conditions. The overestimated scintillation values lead to large tracking error variances which force the receiver to increase the noise bandwidth and hence reduce the receiver performance by allowing more noise to enter the tracking loop. In *Tiwari and Strangeways* [2015], the overestimation factor in the case of $\sigma_{\phi a}$ was leading to large tracking error variances which in future can be reduced by using the $\sigma_{\phi a}^{w}$ index.

4. Conclusion

A new improved analogous phase scintillation index ($\sigma_{\phi a}^{w}$) is presented in this paper using a wavelet-transform-based filtering method to better represent the phase scintillation activity at European high latitudes. The improper filtering effects in the case of the previously proposed analogous phase index and the actual phase scintillation index was resulting in both overestimated and underestimated scintillation

values especially for moderate to weak scintillation conditions. It is shown in this paper that the new proposed index can be used in all geomagnetic conditions as it has shown a good correlation with the previously proposed analogous phase index and the actual phase scintillation index. The main reason to propose the improved version of the previously proposed $\sigma_{\phi a}$ index was its low computational cost since it uses the TEC measurements at 1 Hz rather than the 50 Hz data used in the conventional scintillation receivers for which the necessary calculations are much more computationally intensive. This makes $\sigma_{\phi a}^{w}$ a very good candidate for estimating the tracking error variance so that in future it can be effectively used for updating the tracking loop parameters of a GPS receiver during weak to strong scintillation conditions. The index can also be used as a regional alarming index for representing the phase scintillation activity at European high latitudes. In future, the performance of the $\sigma_{\phi a}^{w}$ will be validated by using the data from other stations at European high-latitude stations and also by using the data from the Canadian high latitudes.

Acknowledgments
The authors (R. Tiwari and H.J. Strangeways) wish to acknowledge the EPSRC (Engineering and Physical Science Research Council) for financial support for some of this work through grant EP/H004637/1. The first author also thanks IBA, Sukkur, Pakistan, for providing the funding for his PhD studies. The authors are also grateful to the Geospatial Institute at Nottingham University, UK, for use of archived GPS data collected under linked EPSRC grants for scintillation modeling and mitigation between Newcastle, Nottingham, and Bath Universities. We also thank World Data Center (WDC) for Geomagnetism and Kyoto for *Kp* data.

References

Aarons, J. (1977), Equatorial scintillations: A review, *IEEE Trans. Antennas Propag.*, *25*(5), 729–736.
Aarons, J. (1997), Global Positioning System phase fluctuations at auroral latitudes, *J. Geophys. Res.*, *102*(17), 219–231.
Aarons, J., B. Lin, M. Mendillo, K. Lio, and M. Codrescue (2000), Global Positioning System phase fluctuation and ultraviolet images from the polar satellite, *J. Geophys. Res.*, *105*(3), 5201–5213.
Basu, S., E. J. Weber, T. W. Bullet, M. J. Keskinen, E. MacKenzie, P. Doherty, R. Sheeham, H. Kuenzler, P. Ning, and J. Bongiolatti (1998), Characteristics of plasma structuring in the cusp/cleft region at Svalbard, *Radio Sci.*, *33*(6), 1885–1899.
Basu, S., K. Grovesa, J. Quinna, and P. Dohertyb (1999), A comparison of TEC fluctuations and scintillations at Ascension Island, *J. Atmos. Sol. Terr. Phys.*, *61*(16), 1219–1226.
Beach, T. B., and P. M. Kintner (1999), Simultaneous Global Positioning System observations of equatorial scintillations and total electron content fluctuations, *J. Geophys. Res.*, *104*, 22,553–22,565.
Cleff, T. (2009), *Exploratory Data Analysis in Business and Economics: An Introduction Using SPSS, Stata, and Excel*, Springer, Switzerland.
Datta-Barua, S., P. Doherty, S. Delay, T. Dehel, and J. Klobuchar (2003), Ionospheric scintillation effects on single and dual frequency GPS positioning, paper presented at 16th International Technical Meeting of the Satellite Division of The Institute of Navigation (ION GPS/GNSS 2003), pp. 336–346, Portland, Oregon, 9–12 Sept.
Doherty, P. H., S. H. Delay, C. E. Valladares, and J. A. Klobuchar (2000), Ionospheric scintillation effects in the equatorial and auroral regions, paper presented at 13th International Technical Meeting of the Satellite Division of The Institute of Navigation (ION GPS 2000), pp. 662–671, Salt Lake City, Utah, 19–22 Sept.
Forte, B. (2005), Optimum detrending of raw GPS data for scintillation measurements at auroral latitudes, *J. Atmos. Sol. Terr. Phys.*, *67*(12), 1100–1109, doi:10.1016/j.jastp.2005.01.011.
Forte, B. (2007), On the relationship between the geometrical control of scintillation indices and the data detrending problems observed at high latitudes, *Ann. Geophys.*, *50*(6), 699–706.
Garner, T. W., T. L. Gaussiran II, B. W. Tolman, R. B. Harris, R. S. Calfas, and H. Gallagher (2008), Total electron content measurements in ionospheric physics, *Adv. Space Res.*, *42*(4), 720–726.
Ghoddousi-Fard, R., P. Prikryl, and F. Lahaye (2013), GPS phase difference variation statistics: A comparison between phase scintillation index and proxy indices, *Adv. Space Res.*, *52*(8), 1397–1405.
Guozhu, L., N. Baiqi, R. Zhipeng, and H. Lianhuan (2008), Statistics of GPS ionospheric scintillation and irregularities over polar regions at solar minimum, *GPS Solut.*, *14*, 331–341, doi:10.1007/s10291-009-0156-x.
Jakowski, N., C. Borries, and V. Wilken (2012), Introducing a disturbance ionosphere index, *Radio Sci.*, *47*, RS0L14, doi:10.1029/2011RS004939.
Kersley, L., S. E. Pryse, and N. S. Wheadon (1988), Amplitude and phase scintillation at high latitudes over northern Europe, *Radio Sci.*, *23*(3), 320–330.
Kintner, P. M., B. M. Ledvina, and E. R. de Paula (2007), GPS and ionospheric scintillations, *Space weather*, *5*, S09003, doi:10.1029/2006SW000260.
Knight, M. F. (2000), Ionospheric scintillation effects on global positioning system receivers, PhD thesis, Adelaide, South Australia.
Krankowski, A., I. Shagimuratov, I. Lubomir, W. Baran, and I. I. EphishoV (2005), Study of TEC fluctuations in Antarctic ionosphere during storm using GPS observations, *Acta Geophys. Apolonica*, *53*(2), 205–218.
Materassi, M., and C. N. Mitchell (2007), Wavelet analysis of GPS amplitude scintillation: A case study, *Radio Sci.*, *42*, RS1004, doi:10.1029/2005RS003415.
Materassi, M., and C. N. Mitchell (2009), Detrend effect on the scalograms of {GPS} power scintillation, *Adv. Space Res.*, *43*(11), 1740–1748.
Mushini, S. C., P. T. Jayachandran, R. B. Langley, J. W. MacDougall, and D. Pokhotelov (2012), Improved amplitude- and phase-scintillation indices derived from wavelet detrended high-latitude GPS data, *GPS Solut.*, *16*(3), 363–373.
Niu, F., Y. Morton, J. Wang, and W. Pelgrum (2012), GPS carrier phase detrending methods and performances for ionosphere scintillation studies, paper presented at 25th International Technical Meeting of the Satellite Division of The Institute of Navigation, ION GNSS 2000, pp. 1462–1467, Newport Beach, Calif., 30–31 Jan.
Prikryl, P., P. T. Jayachandran, S. C. Mushini, and I. G. Richardson (2012), Toward the probabilistic forecasting of high-latitude GPS phase scintillation, *Space Weather*, *10*, S08005, doi:10.1029/2012SW000800.
Prikryl, P., R. Ghoddousi-Fard, B. S. R. Kunduri, E. G. Thomas, A. J. Coster, P. T. Jayachandran, E. Spanswick, and D. W. Danskin (2013), GPS phase scintillation and proxy index at high latitudes during a moderate geomagnetic storm, *Ann. Geophys.*, *31*(5), 805–816.
Prikryl, P., P. Jayachandran, S. Mushini, and I. Richardson (2014), High-latitude GPS phase scintillation and cycle slips during high-speed solar wind streams and interplanetary coronal mass ejections: A superposed epoch analysis, *Earth Planets Space*, *66*(1), 62.
Seo, J., T. Walter, T. Chiou, and P. Enge (2009), Characteristics of deep GPS signal fading due to ionospheric scintillation for aviation receiver design, *Radio Sci.*, *44*, RS0A16, doi:10.1029/2008RS004077.
Skone, S., M. Feng, F. Ghafoori, and R. Tiwari (2008), Investigation of scintillation characteristics for high latitude phenomena, paper presented at 21st International Technical Meeting of the Satellite Division of The Institute of Navigation (ION GNSS 2008), pp. 2425–2433, Savannah, Georgia, 16–19 Sept.

Skone, S., M. Feng, R. Tiwari, and A. Coster (2009), Characterizing ionospheric irregularities for auroral scintillation, paper presented at 22nd International Technical Meeting of The Satellite Division of the Institute of Navigation (ION GNSS 2009), pp. 2551–2558, Savannah, Georgia, 22–25 Sept.

Starck, J.-L., F. Murtagh, and A. Bijaoui (1998), *Image Processing and Data Analysis: The Multiscale Approach*, Cambridge Univ. Press, New York.

Tiwari, R., and H. J. Strangeways (2015), Regionally based alarm index to mitigate ionospheric scintillation effects for GNSS receivers, *Space Weather*, *13*, 72–85, doi:10.1002/2014SW001115.

Tiwari, R., F. Ghafoori, O. Al-Fanek, O. Haddad, and S. Skone (2010), Investigation of high latitude ionospheric scintillations observed in the Canadian Region, paper presented at 23rd International Technical Meeting of The Satellite Division of the Institute of Navigation (ION GNSS 2010), pp. 349–360, Portland, Oregon, Sept.

Tiwari, R., S. Tiwari, P. K. Purohit, and A. K. Gwal (2011a), Navigation with global positioning system in Antarctic circle, in *Antarctica: The Most Interactive Ice-Air-Ocean Environment*, edited by J. Singh and H. Dutta, pp. 233–248, Nova Sci., Hauppauge, N. Y.

Tiwari, R., H. J. Strangeways, S. Tiwari, S. Boussakta, and S. Skone (2011b), GPS L1 phase scintillation using wavelet analysis at high latitude, paper presented at 7th IEEE International Workshop on Systems, Signal Processing and their Applications (WOSSPA), pp. 227–230, Tipaza, Algeria, 9–11 May.

Tiwari, R., H. J. Strangeways, S. Tiwari, and A. Ahmed (2013), Investigation of ionospheric irregularities and scintillation using TEC at high latitude, *Adv. Space Res.*, *52*(6), 1111–1124.

Torrence, C., and G. P. Compo (1998), A practical guide to wavelet analysis, *Bull. Am. Meteorol. Soc.*, *79*(1), 61–78, doi:10.1175/1520-0477.

Van Dierendonck, A. J., and B. Arbesser-Rastburg (2004), Measuring ionospheric scintillation in the equatorial region over Africa, including measurements from SBAS geostationary satellite signals, paper presented at 17th International Technical Meeting of the Satellite Division of The Institute of Navigation (ION GNSS 2004), pp. 316–324, Long Beach, Calif., 21–24 Sept.

Van Dierendonck, A. J., J. Klobuchar, and Q. Hua (1993), Ionospheric scintillation monitoring using commercial single frequency C/A code receivers, paper presented at 6th International Technical Meeting of the Satellite Division of The Institute of Navigation (ION GPS 1993), pp. 333–34, Salt Lake City, UT, 22–24 Sept.

Xu, R., Z. Liu, M. Li, Y. Morton, and W. Chen (2012), An analysis of low-latitude ionospheric scintillation and its effects on precise point positioning, *J. Global Positioning Sys.*, *11*(1), 22–32.